High-Q 100 ghz photonic crystal resonator fabricated from a cyclic olefin copolymer

Salek, Milan; Hanham, S. M.; Gregory, Andrew

DOI:
10.1109/LMWC.2022.3186168

High-Q 100 GHz Photonic Crystal Resonator Fabricated from a Cyclic Olefin Copolymer

Milan Salek, Stephen M. Hanham, *Senior Member, IEEE* and Andrew P. Gregory

***Abstract*—This letter describes the design, fabrication, and characterization of an air-mode 1D photonic crystal resonator (PCR) operating at 100 GHz. The PCR was fabricated from an inexpensive cyclic olefin copolymer (COC) using computer numerical control (CNC) milling. It is demonstrated that despite the lack of complete electromagnetic bandgap arising due to the low permittivity of the COC, it remains possible to realize a resonator with a high-quality factor (Q-factor) of 2800 through shaping of the resonant field to minimize radiative loss.**

***Index Terms*—CNC milling, cyclic olefin copolymer, photonic crystal resonator, Q-factor, resonator.**

I. INTRODUCTION

PHOTONIC crystal resonators (PCRs) have numerous advantages compared to other types of cavity resonators, most notably high Q-factors limited only by dielectric loss combined with small resonant mode volumes [1-4]. Widely used in the optical domain, they have more recently been developed for the millimeter-wave (mm-wave) and terahertz bands with 1D [5] and 2D [6], [7] realizations fabricated from high resistivity silicon. Their high Q-factor, planar geometry and ability to be integrated with dielectric slab waveguides (DSWs) makes them promising for use in future low loss filters, low phase noise oscillators and as sensing platforms (e.g. [8]) in the mm-wave and terahertz bands.

This paper presents the design, fabrication and characterization of a 100 GHz 1D PCR fabricated from a cyclic olefin copolymer (COC) whose Q-factor exceeds a conventional metal cavity resonator. The particular COC employed is a thermoplastic called Topas [9], which is produced by the chain copolymerization of norbornene with ethylene. The motivation for using this dielectric material is the very low dielectric loss (i.e. loss tangent $\tan\delta < 10^{-3}$) in the mm-wave and sub-terahertz frequency ranges [10], allowing high resonator Q-factors. Additionally, this material is inexpensive (particularly when compared to the alternative high resistivity silicon), has low water absorption (<0.01%) and high optical transmission. The material has a relatively low real permittivity ($\epsilon_r' = 2.34$), which would commonly be viewed as a barrier for its use as an electromagnetic bandgap material [11]. However, in this letter we demonstrate how this may be overcome in the case of a 1D PCR where an incomplete bandgap is present in the dispersion properties of its constituent unit cells. The remainder of the letter is organized as follows. Sections II and III describe the design process of the PCR and its fabrication using CNC milling, respectively. Section IV presents the characterization of the device, analysis and discussion.

II. DEVICE DESIGN

A. Resonator Design

The PCR shown in Fig. 1 consists of a dielectric slab waveguide (DSW) containing a linear array of $2N = 72$ cylindrical air holes to support a *TE* Bloch mode. The holes with radius $r = 0.3$ mm and period $a = 1.12$ mm are distributed symmetrically about the $x = 0$ plane. To confine a resonant mode to the center of the DSW, the width of the waveguide $b(x)$ is quadratically tapered from the center to the ends according to $b(x) = -6.15 \times 10^{-4}x^2 + 3.2$, where $x \in [-Na, Na]$ and the dimensions are in millimeters. The electromagnetic properties of the waveguide forming the resonator may be analyzed using the *locally periodic approximation* where each section of waveguide with an air hole is treated as a unit cell (shown in the inset of Fig. 2(a)) with infinite periodicity in the $\pm x$-directions [12]. Fig. 2(a) shows the calculated band diagram for the *TE* Bloch modes of a central unit cell ($x \in [0, a/2]$) calculated using $\pm x$ periodic boundary conditions with the MIT Photonic Bands (MPB) software package which utilizes conjugate-gradient minimization of the block Rayleigh quotient on a plane-wave basis to calculate the unit cell eigenmodes [13]. The Bloch mode used by the resonator is mode 2 (colored cyan in Fig. 2(a)), commonly referred to as the *air mode* since the electric field concentrates (but not exclusively) in the air regions rather than the dielectric regions, reducing dielectric loss [7], [11]. It can be observed from Fig. 2(a) that a complete *TE* bandgap, which is often viewed as a prerequisite for realizing a PCR, does not exist between modes 1 and 2. Here, we demonstrate that a resonator may still be realized despite the lack of a complete bandgap which can be difficult to engineer from materials with a low real permittivity [14].

Manuscript received March 14, 2022; revised May 26, 2022; accepted June 14, 2022. Date of publication xxx, 2022; date of current version June 14, 2022. The work was supported by the U.K. Engineering and Physical Science Research Council (EPSRC) under Contract EP/V001655/1. For the purpose of open access, the author(s) has applied a Creative Commons Attribution (CC BY) license to any Accepted Manuscript version arising. Data supporting this publication is available at https://doi.org/10.25500/edata.bham.00000850.

(Corresponding author: Stephen Hanham).

M. Salek and S. M. Hanham are with the Department of Electronic, Electrical and Systems Engineering, University of Birmingham, Birmingham B15 2TT, U.K. (e-mail: m.salek@bham.ac.uk; stephen.hanham@ieee.org).

A. P. Gregory is with the National Physical Laboratory, Teddington, Middlesex, TW11 0LW, U.K. (e-mail: andrew.gregory@npl.co.uk).

Digital Object Identifier

The tapering of the waveguide width from the center towards the ends has the effect of progressively increasing the frequencies of the unit cell eigenmodes, confining a mode 2 resonance to the center of the waveguide. The quadratic shape of the tapering profile is chosen to achieve a Gaussian envelope of the resonant mode's field as discussed in [12], [15]. The tapering length is chosen as a tradeoff between the length of the device and minimizing the radiative loss of the resonator, characterized by the radiation Q-factor Q_{rad}. Increasing the taper length reduces the wavevector components of the resonant mode field inside the light cone which contributes to radiative loss. Ideally, Q_{rad} is chosen to be much greater than the Q-factor associated with dielectric loss Q_{mat} to achieve a material loss limited Q-factor. The tapering also ensures that the resonance field does not contain wavevector components corresponding to other eigenmodes at the resonant frequency to avoid mode coupling. Fig. 2(b) shows how the extended taper length causes the power spectral density of the wavevector component k_x of the resonant mode field to be narrowly concentrated about the irreducible Brillouin zone edge $k_x = \pi/a$, away from the light cone and other modes. Resonant mode 2 has even symmetry about the x-axis for the dominant electric field component E_y, whereas modes 3 and 4 have odd symmetry, making them unlikely to couple (in addition to not satisfying the phase match condition as previously described).

Full-wave electromagnetic simulations of the device were performed using the finite-element method (FEM) solver in CST Microwave Studio [16]. For the simulations, the relative permittivity of the Topas was set to $\epsilon_r = \epsilon_r'(1 - j\tan\delta)$ where $\epsilon_r' = 2.34 \pm 0.01$ and $\tan\delta = (2.62 \pm 0.24) \times 10^{-4}$ based on measurements of a COC wafer by the National Physical Laboratory (NPL) U.K. using a 72 GHz open cavity resonator and calculated using expanded uncertainties with coverage factor $k = 2$. Note that these values are close to the permittivity reported in [17] at 300 GHz indicating negligible dispersion in the COC permittivity. Fig. 2(c) shows the electric field distribution of the PCR for the fundamental mode resonance.

B. PCR Mounting and Enclosure

The PCR is suspended using four supporting beams of width $w_{sb} = 5.6$ mm and length $l_{sb} = 5.6$ mm, shown in Fig. 1(d), to electromagnetically isolate the resonant mode's field from its surroundings, minimizing leakage and scattering losses. The supporting beams are perforated with a dense lattice of cylindrical air holes with sub-wavelength diameter $h_d = 0.35$ mm ($0.12\lambda_0$, where λ_0 is the free-space wavelength) and period $h_a = 0.4$ mm ($0.14\lambda_0$) to create an effective medium with a low permittivity as described in [18]. This approach leads to minimal scattering of the fundamental TE_0 guided mode on the DSW by the support beams. The PCR and supports are fabricated as a single piece of COC with uniform thickness 2.5 mm.

Tapered sections at both ends of the DSW along with flaring metallic horn structures are used to form a low loss transition between the DSW and WR-10 metal rectangular waveguides as shown in Fig. 1(c). Here, the tapered ends of the DSW partially protrude into the aperture of the horn structure and transition

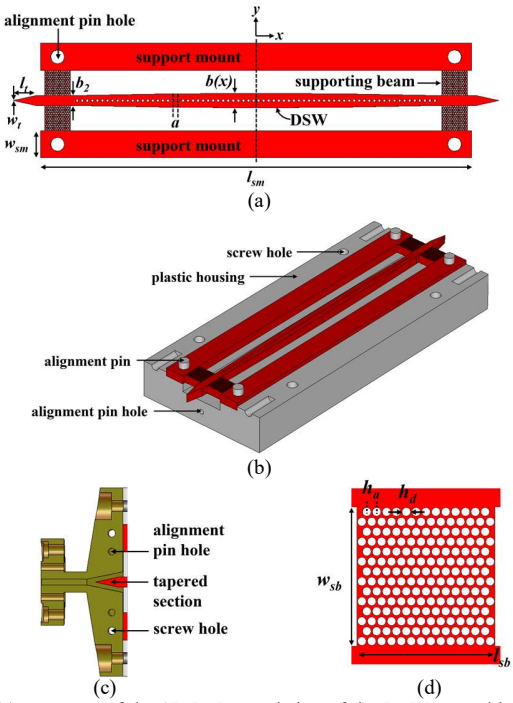

Fig. 1. (a) Structure of the 1D PCR consisting of the DSW central beam with support mounts and supporting beams. (b) Structure of the plastic housing showing how the PCR is mounted above the groove within the housing. Note that the top part of the plastic housing is not shown here. (c) Enlarged view of the tapered DSW section and bottom half of the metallic horn structure used as a transition between the DSW and WR-10 waveguide. The flange is a standard UG387/U flange. (d) Enlarged view of one of the supporting beams.

linearly from the DSW end width of $b_2 = 2.2$ mm to a width of $w_t = 0.02$ mm over a length of $l_t = 5$ mm. A simulation of the back-to-back transition between the WR-10 waveguide and the DSW shows the total loss (S_{21}) is 0.39 dB, excluding material losses.

III. DEVICE FABRICATION

The PCR shown in Fig. 3(a) was fabricated using CNC milling of a single injection molded Topas wafer [9] with diameter 115 mm and thickness 2.5 mm. The PCR was enclosed in a housing constructed from CNC milled acrylic and split in the $z = 0$ plane to allow the PCR to be mounted as shown in Fig. 3(b) and 3(c). The PCR and two halves of the housing are then aligned using four alignment pins and fixed using four M3 nuts and bolts. The WR-10 flange, and horn sections were CNC milled from brass in two halves and aligned using two vertical alignment pins and fixed using two M1.6 nuts and bolts. Each flange and horn section were fixed to the housing using two M3 bolts and aligned using two horizontal alignment pins.

IV. CHARACTERIZATION AND DISCUSSION

The *S*-parameter measurements of the device were performed using a Keysight PNA-X N5247B vector network analyzer with Keysight N5295AX03 frequency extension modules and coaxial to waveguide adaptors. The system was calibrated at the waveguide flanges of the adaptors using a through-reflect-line calibration scheme. Fig. 4 shows the measured and simulated scattering parameters of the device across the frequency range

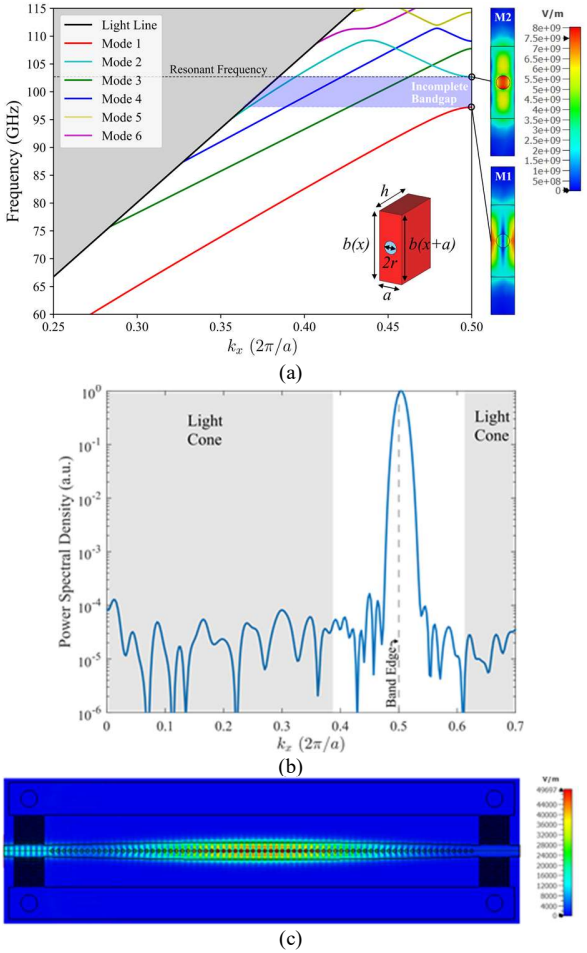

Fig. 2. (a) Transverse-electric (*TE*) mode band diagram for one of the central unit cells of the PCR with the electric field shown for modes 1 (M1) and 2 (M2). (b) Power spectral density of the wavevector component k_x of the resonant mode's magnetic field component H_z. (c) Simulated electric field distribution of the fundamental resonant mode in the $z = 0$ plane.

of 100 – 110 GHz. The visible peaks in S_{21} represent the first six resonant modes with the fundamental resonance at the lowest frequency $f_0 = 103.48$ GHz. There is good agreement between simulated and measured results with only a 32 MHz difference in the fundamental resonance frequency. The average thickness of the fabricated PCR was measured to be 2.513 mm and based on a tolerance analysis in CST this 13 µm increase in PCR thickness explains the ~32 MHz frequency shift.

The loaded Q-factor Q_l of the PCR was calculated from the full-width at half-maximum (FWHM) frequency bandwidth of the measured S_{21} to be 2800, which compares well with the simulated value of 3410, accounting for fabrication tolerances. The experimental unloaded Q-factor of the resonator may be estimated to be $Q_{ul} = Q_l/(1 - |S_{21}(f = f_0)|) = 3700$ (assuming leakage through the resonator is negligible). In theory, a material loss limited design would have a loaded Q-factor $Q_l = Q_{mat} = (\rho \tan\delta)^{-1} = 4710$, where $\rho = 0.81$ is the calculated dielectric filling factor of the resonant mode. These results indicate the potential for higher Q-factors through improved fabrication and the introduction of additional unit cells for increased waveguide decoupling at the expense of

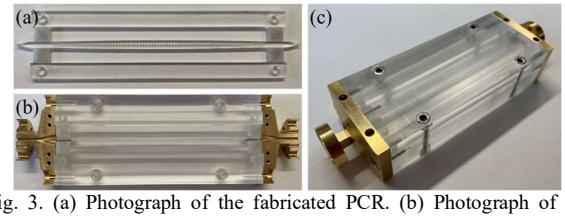

Fig. 3. (a) Photograph of the fabricated PCR. (b) Photograph of the PCR mounted in the bottom half of the housing with flange and horn sections attached. (c) Photograph of the fully assembled device.

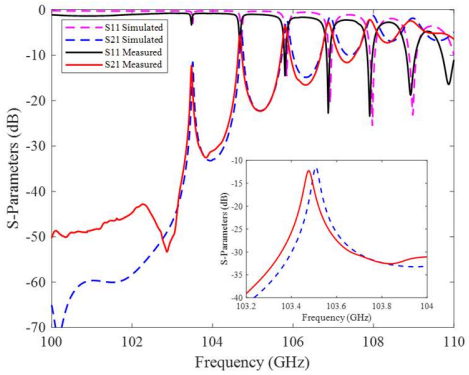

Fig. 4. Measured and simulated *S*-parameter of the device. The inset shows an enlarged view of S_{21} for the fundamental resonant mode. Unloaded Q-factors of the first three resonant modes are: 4620, 4420 and 3890.

TABLE I
MM-WAVE RESONATOR TECHNOLOGIES

f_c (GHz)	R.T.	Q_u	S.M.S.D. (%)	M.T.	*Ref.*
87.86	MW	573	40	L.I.S.G.	[19]
183	MW	648	33	3D Printing	[20]
101.14	MW	741	56	3D Printing	[21]
117.1	MW	830	12	CNC Milling	[22]
106.8	PCR	11900	2	Si.Mic.	[5]
103.476	PCR	3700	1.2	CNC Milling	T.W.

f_c: operating frequency; R.T.: resonator type (MW: metallic waveguide; PCR: photonic crystal resonator); Q_u: stated or estimated unloaded Q-factor; S.M.S.D.: spurious mode spectral distance; M.T.: manufacturing technique (L.I.S.G.: laser induced structured glass; Si.Mic.: silicon micromachining); T.W.: this work; Ref.: reference.

reduced forward transmission S_{21} and increased device length.

A disadvantage of the use of a lower permittivity material for a 1D PCR is the required increase in the length of the device, particularly when compared to silicon devices (see [5]), and the close spacing of the higher order modes. Table I describes the performance for representative resonators at similar mm-wave frequencies. The reported resonator has a favorable performance in terms of Q-factor with the advantage of being fabricated from an inexpensive material.

V. CONCLUSION

This letter demonstrated the design, fabrication, and characterization of an air-mode 1D PCR fabricated from a COC material using CNC milling. Despite the low relative permittivity of the material and resulting lack of a complete *TE* band gap, a high loaded Q-factor resonance of 2800 was realized. The results demonstrate the potential of the use of inexpensive COCs for realizing future low loss and high Q-factor mm-wave and terahertz components such as filters, oscillators and sensors.

REFERENCES

[1] Y. Akahane, T. Asano, B. S. Song, and S. Noda, "High-Q photonic nanocavity in a two-dimensional photonic crystal," *Nat.*, vol. 425, no. 6961, pp. 944–947, Oct. 2003, doi: 10.1038/nature02063.

[2] B. S. Song, S. Noda, T. Asano, and Y. Akahane, "Ultra-high-Q photonic double-heterostructure nanocavity," *Nat. Mater.*, vol. 4, no. 3, pp. 207–210, Feb. 2005, doi: 10.1038/nmat1320.

[3] M. Notomi, A. Shinya, S. Mitsugi, E. Kuramochi, and H. Y. Ryu, "Waveguides, resonators and their coupled elements in photonic crystal slabs," Opt. Exp., vol. 12, no. 8, pp. 1551-1561, Apr. 2004, doi: 10.1364/OPEX.12.001551.

[4] M. Notomi, E. Kuramochi, and H. Taniyama, "Ultrahigh-Q Nanocavity with 1D Photonic Gap," *Opt. Exp.*, vol. 16, no. 15, pp. 11095-11102, July 2008, doi: 10.1364/oe.16.011095.

[5] S. M. Hanham, M. M. Ahmad, S. Lucyszyn, and N. Klein, "LED-Switchable High-Q Packaged THz Microbeam Resonators," *IEEE Trans. THz. Sci. Technol.*, vol. 7, no. 2, pp. 199–208, Jan. 2017, doi: 10.1109/TTHZ.2016.2634547.

[6] W. J. Otter, S. M. Hanham, N. M. Ridler, G. Marino, N. Klein, and S. Lucyszyn, "100 GHz ultra-high Q-factor photonic crystal resonators," *Sens. Actuators A: Phys.*, vol. 217, pp. 151–159, Sep. 2014, doi: 10.1016/j.sna.2014.06.022.

[7] E. Akiki *et al.*, "High- Q THz Photonic Crystal Cavity on a Low-Loss Suspended Silicon Platform," *IEEE Trans. THz. Sci. Technol.*, vol. 11, no. 1, pp. 42–53, Aug. 2020, doi: 10.1109/TTHZ.2020.3019928.

[8] S. M. Hanham, C. Watts, W. J. Otter, S. Lucyszyn, and N. Klein, "Dielectric measurements of nanoliter liquids with a photonic crystal resonator at terahertz frequencies," *Appl. Phys. Lett.*, vol. 107, no. 3, pp. 1–6, Jul. 2015, doi: 10.1063/1.4927242.

[9] Microfluidic ChipShop. Accessed: May 23, 2022. [Online]. Available: https://www.microfluidic-chipshop.com/catalogue/polymer-substrates-foils/wafer-format/.

[10] A. Sengupta, A. Bandyopadhyay, B. F. Bowden, J. A. Harrington, and J. F. Federici, "Characterisation of olefin copolymers using terahertz spectroscopy," *Electron. Lett.*, vol. 42, no. 25, p. 1477, Dec. 2006, doi: 10.1049/el:20063148.

[11] J. D. Joannopoulos, S. G. Johnson, J. N. Winn, and R. D. Meade, *Photonic Crystals Molding the Flow of Light*, 2nd ed. Princeton University Press, 2008.

[12] Q. Quan and M. Loncar, "Deterministic design of wavelength scale, ultra-high Q photonic crystal nanobeam cavities," *Opt. Exp.*, vol. 19, no. 19, pp. 18529–18542, Sep. 2011, doi: 10.1364/OE.19.018529.

[13] S. G. Johnson and J. D. Joannopoulos, "Block-iterative frequency-domain methods for Maxwell's equations in a planewave basis," *Opt. Exp.*, vol. 8, no. 3, pp. 173-190, Jan. 2001, doi: 10.1364/oe.8.000173.

[14] R. Gonzalo, B. Martinez, and P. De Maagt, "The effect of dielectric permittivity on the properties of photonic bandgap devices", *Microw. Opt. Technol. Lett.*, vol. 23, no. 2, OCT. 1999, doi: 10.1002/(SICI)1098-2760(19991020)23:2<92::AID-MOP9>3.0.CO;2-J.

[15] Q. Quan, P. B. Deotare, and M. Loncar, "Photonic crystal nanobeam cavity strongly coupled to the feeding waveguide," *Appl. Phys. Lett.*, vol. 96, no. 20, pp. 1–4, May 2010, doi: 10.1063/1.3429125.

[16] Computer Simulated Technology (CST). (2021). Microwave Studio. [Online]. Available: http//www.cst.com/.

[17] L. M. Diaz-Albarran *et al.*, "Development and characterization of cyclic olefin copolymer thin films and their dielectric characteristics as CPW substrate by means of Terahertz Time Domain Spectroscopy," *Microelectronic Engineering*, vol. 191. pp. 84–90, May 2018, doi: 10.1016/j.mee.2018.01.036.

[18] D. Headland, W. Withayachumnankul, X. Yu, M. Fujita, and T. Nagatsuma, "Unclad Microphotonics for Terahertz Waveguides and Systems," *J. Light. Technol.*, vol. 38, no. 24, pp. 6853–6862, Sep. 2020, doi: 10.1109/JLT.2020.3021681.

[19] C. Bartlett, A. Malave, M. Letz, and M. Hoft, "Structured-Glass Waveguide Technology for High-Performance Millimeter-Wave Components and Systems," *IEEE J. Microwaves*, vol. 2, no. 2, pp. 307-315, Mar. 2022, doi: 10.1109/JMW.2022.3155793.

[20] L. Zhu, R. Payapulli, S. H. Shin, M. Stanley, N. M. Ridler, and S. Lucyszyn, "3-D Printing Quantization Predistortion Applied to Sub-THz Chained-Function Filters," *IEEE access*, early access, Mar. 2022. doi: 10.1109/ACCESS.2022.3162586.

[21] C. Bartlett, J. Bornemann, and M. Hoft, "3-D-Printing and High-Precision Milling of W-Band Filter Components With Admittance Inverter Sequences," *IEEE Trans. Compon., Packag. Manuf. Technol.*, vol. 11, no. 12, pp. 2140–2147, Sep. 2021, doi: 10.1109/TCPMT.2021.3116220.

[22] D. Miek, F. Kamrath, P. Boe, and M. Hoft, "T-shaped Dual-Mode Waveguide Filters with Low Manufacturing Complexity for mm-Wave Applications," *2021 IEEE MTT-S Int. Microw. Filter Work. IMFW 2021*, pp. 1–3, Dec. 2021, doi: 10.1109/IMFW49589.2021.9642330.